



RESEARCH ARTICLE

Gas-Phase Fluorescence Excitation and Emission Spectroscopy of Three Xanthene Dyes (Rhodamine 575, Rhodamine 590 and Rhodamine 6G) in a Quadrupole Ion Trap Mass Spectrometer

Matthew W. Forbes, Rebecca A. Jockusch

Department of Chemistry, University of Toronto, Toronto, ON, M5S 3H6, Canada

Abstract

The gas-phase fluorescence excitation, emission and photodissociation characteristics of three xanthene dyes (rhodamine 575, rhodamine 590, and rhodamine 6G) have been investigated in a quadrupole ion trap mass spectrometer. Measured gas-phase excitation and dispersed emission spectra are compared with solution-phase spectra and computations. The excitation and emission maxima for all three protonated dyes lie at higher energy in the gas phase than in solution. The measured Stokes shifts are significantly smaller for the isolated gaseous ions than the solvated ions. Laser power-dependence measurements indicate that absorption of multiple photons is required for photodissociation. Redshifts and broadening of the dispersed fluorescence spectra at high excitation laser power provide evidence of gradual heating of the ion population, pointing to a mechanism of sequential multiple-photon activation through absorption/emission cycling. The relative brightness in the gas phase follows the order R575 (1.00) < R590 (1.15) < R6G (1.29). Fluorescence emission from several mass-selected product ions has been measured.

Key words: Fluorescence, Quadrupole ion trap mass spectrometry, Photodissociation, Rhodamine

Introduction

Fluorescence excitation and emission spectroscopy combined with mass-resolved photodissociation measurements provides a platform to probe the intrinsic photophysical properties of gas-phase chromophores, free from any interfering effects of solvent. Recently, our group [1–4] and several

others [5–24] have presented works focusing upon the development, characterization and applications of instrumentation for measuring laser-induced fluorescence from molecular ions in the gas phase. The majority of these studies have used highly fluorescent molecules such as the xanthene-based rhodamine dyes. The instrumentation developed features laser light sources coupled into trapping mass spectrometers that are used to mass-select the ion population of interest and to store the selected ion population for extended periods of time. Several types of mass spectrometers have been employed, including 3-D Paul-type quadrupole ion traps (QIT) [1–17], Fourier transform ion cyclotron resonance mass spectrometers (FT-ICR-MS) [18–23], and linear radiofrequency ion traps

Electronic supplementary material The online version of this article (doi:10.1007/s13361-010-0017-4) contains supplementary material, which is available to authorized users.

Correspondence to: Rebecca A. Jockusch; e-mail: rebecca.jockusch@utoronto.ca

Received: 3 June 2010
Revised: 1 September 2010
Accepted: 7 September 2010
Published Online: 28 January 2011

(LIT) [24]. Detection of integrated gas-phase fluorescence has been accomplished using high-sensitivity photomultiplier tubes [5–7, 9–11, 13–17, 21–24] or avalanche photodiodes [18, 19, 25], while dispersed fluorescence has been measured using spectrographs with charge-coupled device (CCD) detectors [1–4, 8, 12, 22].

Measurements of the intrinsic photophysical properties of gaseous chromophores provide both a benchmark for the validation and calibration of electronic structure theory calculations and a baseline from which to better understand the effects of solvent interactions. Another promising application of gas-phase fluorescence spectroscopy is to provide a probe of the conformations and dynamics of biologically relevant ions such as proteins, peptides and noncovalent protein/ligand complexes through the use of Förster resonance energy transfer (FRET) [6, 25–27] or fluorescence contact quenching [7–10].

Perhaps the first optical investigation of charged particles in an electrodynamic trap was from the work of Wuerker et al., who photographed the Lissajous trajectories of charged aluminum dust particles in a Paul-type ion trap [28]. It was not until the late 1970s, however, that Dehmelt and coworkers measured fluorescence emission from a mass-selected population of Ba^+ ions in a QIT [29, 30]. Shortly thereafter, Werth and coworkers observed the time-resolved fluorescence decay of Ba^+ using a pulsed dye laser and investigated the effect of helium bath gas pressure on the computed fluorescence lifetimes [31]. Since that time, there have been numerous reviews detailing progress in this field of spectroscopy, including measurements of hyperfine spectra of heavy atomic ions, methods for cooling trapped ions (including collisional, resistive, and laser cooling techniques) and observations of quantum jumps through electron shelving, single ion spectroscopy [32–37].

Fluorescence in ion traps remained largely focused upon very small molecular and atomic ions until 2001, when Wang et al. measured the gas-phase fluorescence excitation spectrum of hexafluorobenzene cations confined and mass-selected in the Penning cell of an FT-ICR mass spectrometer [21]. Also using an FT-ICR, Cage et al. reported resolved fluorescence emission spectra from trifluorobenzene cations [22].

Khoury et al. [5] showed the first fluorescence measurements from molecular ions of organic dyes produced via electrospray ionization in a home-built quadrupole ion trap. The dyes investigated in that study were Alexfluor 350 and rhodamine 640 (also known as rhodamine 101). Using a pulsed laser, Khoury et al. measured fluorescence via photon counting under zero-background conditions. The fluorescence yield from these dyes was investigated as a function of spatial displacement in the QIT (in both the axial and radial directions), the size of the trapped ion population, and the trapping parameter q_z . Additionally, the rate of photofragmentation was compared directly with the temporal decay of the measured fluorescence intensity.

Shortly thereafter, Wright et al. [12] presented results showing dispersed fluorescence measurements and the

photodissociation of rhodamine 6G (R6G) and 5-carboxy-R6G in a modified QIT. The fluorescence yield was investigated with respect to laser power, trapping conditions (q_z), and ion population. In particular, Wright et al. highlighted the dramatic effect of He bath gas pressure on the measured fluorescence yield. Elevating the pressure of the buffer gas in the QIT results in higher rates of collisional cooling, thereby suppressing photofragmentation processes and allowing for the use of higher laser powers to increase fluorescence signals. The gas-phase fluorescence and photodissociation of several other rhodamine dyes have subsequently been investigated by our group [1, 2, 4] and others [17–20, 25, 38].

In a series of elegant experiments, Parks and coworkers designed a number of dye-labeled molecules implementing FRET and fluorescence contact quenching to probe changes in the conformation and dynamics of biologically relevant ions produced by ESI. These studies included an investigation of the temperature-induced melting of dye-labeled double-stranded DNA [6], as well as fluorescence quenching in the Trp-cage protein [7, 10] and dye-labeled polypeptides [8, 9, 11].

An important early step in the development of gas-phase FRET methodology is the identification and characterization of the intrinsic properties of appropriate donor and acceptor fluorophore pairs. While the properties of many fluorophores in the condensed phase are well known, their gas-phase properties may be quite different because the fluorophore's local environment can play an enormous role in determining its absorption, emission and lifetime characteristics [39]. Indeed, several previous fluorescence studies of gas-phase ions have highlighted the extent to which solvation can promote bathochromic shifts in the excitation and emission maxima of xanthene dyes [2, 5, 12]. More dramatic differences in fluorescence may also exist between gaseous and solvated molecules; for example, deprotonated fluorescein, which is highly fluorescent in solution, is not a bright fluorophore in the gas phase [2]. Since the intrinsic (i.e., gas-phase) properties of most isolated dyes are not known a priori, the appropriate design, implementation and correct interpretation of gas-phase FRET systems require an understanding of the behavior of each fluorophore independently.

Fluorescence is just one of the de-excitation pathways available to a photoactivated ion; an alternative pathway is dissociation, which can be especially significant in the gas phase. This phenomenon is well known; laser photodissociation of organic chromophores stored in mass spectrometers has been studied extensively since the 1970s, primarily in FT-ICR mass spectrometers [40–43]. Even if a single photon is insufficient to cause fragmentation, photodissociation can still be effected by the gradual buildup of internal energy in a molecule via the absorption of multiple photons, followed rapidly by the intramolecular vibrational redistribution (IVR) of energy. Multiple photon dissociation is a slow process with a rate that depends on the rates of activation and deactivation (both radiative and collisional). Kinetic models describing the

appearance of fragment ions and the disappearance of the precursor ion population as a function of pressure, laser fluence, and photon energy have been explored [17, 38, 40–43]. The ability to observe directly dispersed fluorescence emission of visible light combined with mass-resolved photodissociation measurements provides the opportunity to understand in more detail the competition between fluorescence emission and alternative modes of deactivation.

The photodissociation and fluorescence of several gaseous rhodamine dyes have been examined using different instrumental set-ups. In addition to the work from our group using rhodamine 590 [2, 4], Blades and coworkers [12] examined rhodamine 6G in a quadrupole ion trap, Zenobi and coworkers reported results from several organic dyes [18–20], and Ervin and coworkers [17] presented detailed investigations of the photodissociation and fluorescence of rhodamine 575 in a quadrupole ion trap. In all of these works, investigations were undertaken without the advantage of a continuously tunable light source. Furthermore, among these studies of gaseous rhodamine ions, only the work from Blades' group showed *dispersed* fluorescence spectra [12]. In our laboratory, we have interfaced a quadrupole ion trap mass spectrometer with both a tunable light source and a means of measuring dispersed fluorescence. Here, we use this instrumentation to examine the behavior of a series of rhodamine dyes.

The chemical structures of three closely related rhodamine dyes investigated are shown in Scheme 1: (a) rhodamine 575 (R575), (c) rhodamine 590 (R590), and (d) rhodamine 6G (R6G). These ions differ only by the substitution at the benzoic acid moiety: R575 (also known as R19H⁺) is the free acid, R590 is the methyl ester, and R6G is the ethyl ester. While R590 and R6G are cationic, R575 may exist in solution either as a cation or as a zwitterion (R19[±]), as shown in Scheme 1(b). All of these rhodamines have substantial absorptivities

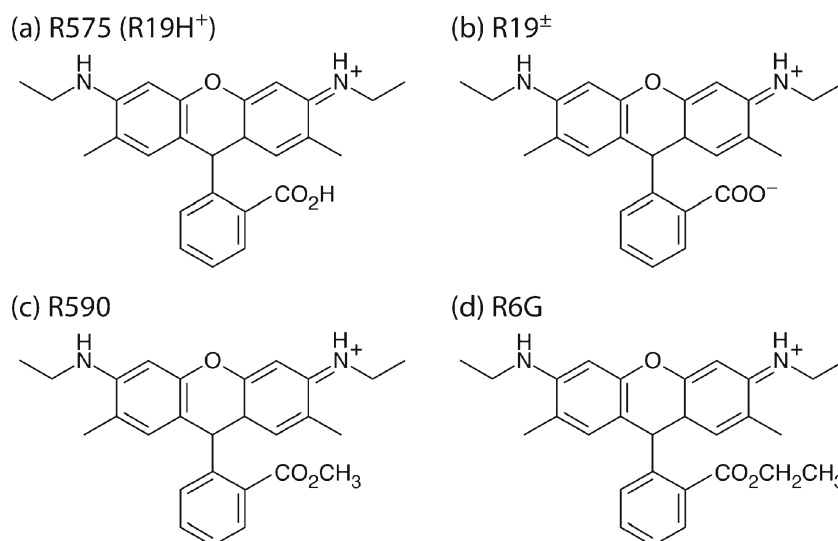
($\sim 80,000 \text{ M}^{-1} \text{ cm}^{-1}$) and high fluorescence quantum yields (Φ_f) in solution, with reported values of 0.82 for R575 [44] and 0.77–0.95 for R6G [44–46].

In this work we present results from a systematic investigation of three rhodamine dyes (Scheme 1) in the gas phase. The intrinsic fluorescence excitation and emission spectra are reported and compared with measurements of these dyes in methanol solutions. The effects of laser power on the dispersed fluorescence emission and mass-resolved photodissociation is investigated. It has been suggested by several authors [4, 12, 17, 20] that fluorescence from fragment ions probably contributes to the observed steady-state laser-induced fluorescence yield of gas phase dyes; therefore, we have utilized the capabilities of the QIT to perform multiple stages of mass spectrometry (MSⁿ) to measure the fluorescence spectra of some interesting fragment ions. Accurate-mass product ion spectra obtained by collision-induced dissociation using a FT-ICR-MS complement the interpretation of the photodissociation spectra and characterization of some fragment ions. Finally, we discuss the effect of increasing laser power on the appearance of the dispersed fluorescence emission spectra and its significance in our understanding of the dynamics of the absorption–emission–photodissociation cycle.

Experimental Methods

Chemicals

The structures of the three rhodamine dyes examined are shown in Scheme 1. Rhodamine 575 (R575) and rhodamine 590 (R590) were obtained from Exciton Corporation (Dayton, OH, USA). Rhodamine 6G was obtained from Sigma-Aldrich (Oakville, ON, Canada). The dyes were dissolved in LC-MS-grade methanol (Mallinckrodt Baker, Inc., Phillips-



Scheme 1. Structures of the rhodamine dyes (a) rhodamine 575 (R575), (b) rhodamine 19 zwitterion (R19[±]); (c) rhodamine 590 (R590), and; (d) rhodamine 6 G (R6G).

burg, NJ, USA) to a concentration of $\sim 0.1 \mu\text{M}$ and electrosprayed by infusion at a flow rate of $\sim 2 \mu\text{L min}^{-1}$.

Solution Spectroscopy

UV/visible excitation and emission spectra of the three dyes were obtained using a PE LS50B spectrofluorometer (Perkin Elmer, Waltham, MA, USA) from solutions in methanol diluted to $\sim 10 \text{ nM}$. Spectra of R575 were also recorded from acidified solutions containing $\sim 0.5\%$ (v/v) HNO_3 . Excitation spectra were recorded by monitoring emission at 580 nm, and emission spectra were recorded with excitation at 480 nm. Monochromator slit bandwidths were 10 nm.

Gas-Phase Laser-Induced Fluorescence

The photodissociation (PD) and fluorescence emission of gas-phase ions were measured using a quadrupole ion trap mass spectrometer (Esquire 3000+, Bruker Daltonik, Bremen, Germany) that was modified for spectroscopy and has already been described [1, 2, 4]. Ions generated by electrospray ionization (ESI) are mass-selected and stored in the QIT (with trapping parameter $q_z=0.6$), where they are irradiated with the frequency-doubled output of an 80 MHz pulsed Ti:Sapphire laser (Tsunami, Spectra-Physics, Mountain View, CA, USA). The laser beam is focused ($1/e^2$ diameter is $\sim 620 \mu\text{m}$, as determined using knife-edge measurements) to the center of the QIT electrode assembly, which it enters and exits through two holes in the ring electrode. Fluorescence is collected through a third hole, orthogonal to path of the laser. The collected fluorescence light is directed through a long-pass filter (Chroma Technology Corp., Rockingham, VT, USA) and focused on the slit ($1500 \mu\text{m}$) of a spectrograph (Shamrock303i, Andor Technologies, Belfast, Ireland), where it is dispersed and detected using an electron-multiplied charge-coupled device (Newton EM-CCD, Andor Technologies). The CCD was cooled to between -60 and -80°C and operated with an EM gain of 255 and a $4\times$ preamp gain.

Mass-selected ions are allowed to cool for 1 s via collisions with room-temperature helium bath gas in the QIT. Then, a single fluorescence emission spectrum was measured by continuous irradiation of the isolated ion population. Following

the irradiation period, the ions are scanned out of the QIT and a mass spectrum is recorded. To obtain a suitable signal-to-noise ratio (S/N), multiple emission spectra (typically twenty) are accumulated from multiple ion populations. The emission spectra are background-subtracted using spectra recorded under identical conditions but with a zero ion population. For comparisons of the fluorescence intensity (e.g., excitation spectroscopy, power dependence, etc.), the integrated fluorescence intensity is taken over the range of wavelengths ($\Sigma\lambda$) indicated in Table 1. Fluorescence measurements are generally obtained from large ion populations, the relative size of which is monitored by the ion charge control (ICC) parameter provided in the instrument software. ICC values are typically in the range of $\sim 1 \times 10^6$. This parameter provides a measure of the relative number of ions stored in the QIT, but does not represent the actual number of stored ions. It is difficult to know precisely the number of ions stored in the QIT, but previous estimates from fluorescence experiments suggest a number of $\sim 5 \times 10^4$ [4]. Table 1 contains a summary of the experimental parameters for each set of measurements described in this work.

MS^3 Fluorescence Experiments

Gas-phase fluorescence spectra were measured for several of the most intense product ions observed from the rhodamine dyes using multiple stages of mass spectrometry (MS^n). Product ions were generated by collision-induced dissociation (CID) in the quadrupole ion trap using dipolar resonant excitation with amplitude V_{AC} (Table 2). Following a 1 s cooling period, irradiation and fluorescence detection proceeded with the same experimental sequence described above. A summary of the experimental parameters for fluorescence detection from the fragment ions is shown in Table 2. CID, rather than photodissociation, was used to produce fragment ions for subsequent fluorescence investigation because in many cases it proved difficult to isolate sufficiently large fragment ion populations via photodissociation. This difficulty is in part a consequence of the fact that fragment ions may themselves photodissociate into second-generation photofragments. Using CID to generate fragments, we have identified several interesting fragment ions from which fluorescence has been detected.

Table 1. A summary of the experimental parameters for the fluorescence and photodissociation experiments

	Excitation spectra	Emission spectra	PD mass spectra	Fluorescence power dependence	PD power dependence
ICC	1.0×10^6	1.0×10^6	3×10^4	1.0×10^6	3×10^4
q_z	0.6	0.6	0.18	0.6	0.6
$P_{\text{He-trap}}$ (mbar)	1.0×10^{-3}	2.3×10^{-3}	0.8×10^{-3}	2.6×10^{-3}	2.6×10^{-3}
t_{ex} (s)	5.0	5.0	3.0	5.0	5.0
t (s)	100.0	1000.0	–	100.0	–
λ_{ex} (nm)	440–510	470	470	470	470
$\Sigma\lambda$ (nm)	510–600	–	–	475–600	–
P (mW)	4.0	4.0	35	0–30.0	0–30.0
Filter	510LP	480LP	–	480LP	–

Table 2. A summary of the experimental parameters used in the MS³ fluorescence emission experiments

	R590→m/z 400	R590→m/z 414	R6G→m/z 415
ICC	1.75 × 10 ⁵	2.25 × 10 ⁵	5.0 × 10 ⁵
q _z	0.6	0.6	0.6
V _{AC}	1.70	1.85	1.45
P _{He,trap} (mbar)	2.3 × 10 ⁻³	2.3 × 10 ⁻³	2.3 × 10 ⁻³
t _{ex} (s)	5.0	5.0	5.0
t (s)	100	500	200
λ _{ex} (nm)	470	470	470
P (mW)	20	20	20
Filter	480LP	480LP	480LP

ICC: ion charge control parameter

q_z: trapping parameter

t_{ex}: irradiation time (s)

t total exposure time (s)

λ_{ex}: excitation wavelength (nm)

P: laser power (mW)

filter: 480 nm or 510 nm long-pass (LP) filter

Photodissociation

Photodissociation mass spectra were obtained from smaller ion populations than those used for fluorescence, with ICC values of $\sim 3 \times 10^4$ to maintain suitable mass resolution and mass accuracy. The photodissociation experiment consists of monitoring the precursor (I_p) and fragment (I_f) ion intensities for multiple ion populations over a period of one to two minutes. The ion intensities during photoexcitation (laser ON) are taken from the average mass spectrum from approximately 25 scans. To obtain an accurate measure of the photodissociation yield (Y), the photodissociation period is bracketed by isolation mass spectra recorded using an identical temporal sequence but with the shutter closed (laser OFF). The precursor ion intensity without photoexcitation (I_p^{OFF}) is taken from the average of these two mass spectra (~ 25 scans). The normalized photodissociation yields of precursor (Y_p) and fragment (Y_f) ions are calculated according to Eqs. 1 and 2:

$$Y_p = \frac{I_p^{ON}}{I_p^{OFF}} \quad (1)$$

$$Y_f = \frac{\sum I_f^{ON}}{I_p^{OFF}} \quad (2)$$

Note that if ions are not lost from the trap upon irradiation, Y_p and Y_f should sum to one (assuming the detector's response is not mass sensitive); however, if ions are lost from the trap (because, for example, a product ion's m/z falls below the low-mass cut-off defined by the storage q_z value), then the sum of Y_f and Y_p will be less than one. Breakdown curves were constructed by plotting Y_p and Y_f as a function of laser power. The unimolecular dissociation rate constant (k_{diss}) is calculated from Y_p and the total irradiation

time (t_{ex}) as in Eq. 3, which assumes pseudo first-order behavior dissociation kinetics [38]:

$$k_{diss} = \frac{-\ln(Y_p)}{t_{ex}} \quad (3)$$

Pressure and q_z

The quadrupole ion trap mass spectrometer is operated with a significant background pressure of helium (He) bath gas to increase the trapping efficiency of externally generated ions, provide spatial focusing, and cool the internal energy of the ion ensemble. The helium pressure in the vacuum chamber is measured using an ionization gauge, which is mounted externally from the quadrupole ion trap electrode assembly. The He pressure is set by adjusting the flow of He leaked directly into the electrode assembly, and is monitored by measuring the increased pressure from He above the base pressure as read by the ionization gauge (corrected for He). We have calculated the conductance and pumping speed for our apparatus to estimate the pressure of He within the ion trap electrode assembly ($P_{He,trap}$) [Forbes, M.W., Nagy, A., Jockusch, R.A.: Photofragmentation and electron photodetachment processes of a GFP model chromophore in a quadrupole ion trap, to be submitted for publication] using a method similar to that reported by other groups [47, 48]. In this work, many experiments were carried out and/or repeated over a period of several months, so there was some variation in the base pressure of the mass spectrometer. However, in all cases where direct comparisons are made amongst the three dyes (for example in the power-dependence experiments), the reported data sets were acquired under comparable instrumental conditions. The helium pressures collected in Table 1 are given as the estimated internal trap pressure ($P_{He,trap}$) which is approximately 140-fold higher than the change in pressure reading on the ionization gauge.

Storing precursor ion populations at high q_z is favorable for fluorescence detection [2, 4, 5, 12, 19, 49] due to an increase in both irradiation efficiency and fluorescence collection efficiency. All of the experiments reported here were conducted at $q_z=0.6$ with the exception of the photodissociation product ion spectra (Figure 4a–c), which were measured at $q_z=0.18$.

High-Resolution Collision-Induced Dissociation MS²

Accurate mass CID spectra of each dye were measured using a hybrid FT-ICR-MS equipped with a 7T magnet (ApexQE, Bruker Daltonics, Billerica, MA, USA). Ions were generated by electrospray, mass-selected with a resolving quadrupole, and fragmented via collisions with Ar gas in a hexapole collision cell. The laboratory-frame collision energy (CE)

was -32 V. High-resolution mass spectra were obtained from the coaddition of 50 time-domain transients of ~ 1 s duration (1 M points). The free induction decay was apodized with a sine function, zero-filled once, and fast Fourier transformed with magnitude calculation. Mass spectra were initially externally calibrated in the range m/z 217–922, providing an average mass error of ~ 0.5 ppm. The use of slightly larger precursor ion populations to observe low-abundance product ions required subsequent internal calibration of the CID spectra. A single-point internal calibration was applied using the known mass of the precursor ion. Further details concerning the mass accuracy can be found in the Electronic Supplementary Material (ESM).

Results and Discussion

Excitation and Emission Spectroscopy

Fluorescence excitation and emission spectra for R575, R590 and R6G are shown in Figure 1. Gas-phase spectra are shown in the top panels (a–c), and solution-phase spectra measured in methanol are shown in the bottom panels (d–f). The excitation and emission maxima ($\lambda_{\text{max}}^{\text{ex}}$, $\lambda_{\text{max}}^{\text{em}}$) are

indicated, and observed spectral features are summarized in Table 3. There is remarkable similarity in both the appearance and band positions of these three dyes in the gas phase. $\lambda_{\text{max}}^{\text{ex}}$ and $\lambda_{\text{max}}^{\text{em}}$ are indistinguishable between R590 and R6G. For R575, the free acid, $\lambda_{\text{max}}^{\text{ex}}$ is shifted -100 cm^{-1} to lower energy and $\lambda_{\text{max}}^{\text{em}}$ is shifted -80 cm^{-1} compared to the methyl and ethyl esters. The gas-phase excitation and emission spectra also demonstrate excellent mirror-image quality. Shoulders are clearly evident in both the excitation and the emission profiles, indicating the existence of at least two transitions of reasonable oscillator strength between S_0 and S_1 . Furthermore, similar spacings are seen between the maximum and the shoulder (ΔE_{0-1}) of the excitation and emission spectra for each dye. In solution, shoulders are evident in the excitation profiles, but these features are largely absent in the emission spectra; thus, although excitation to a vibrationally excited level of S_1 is observed, it appears that the probability of a transition from S_1 to an excited vibrational level of S_0 is lower in solution than in the gas phase.

Perhaps the most striking feature of these spectra is that for each dye, solvation in methanol gives rise to a significant bathochromic (red)shift in both the excitation and emission spectra (i.e., the $S_0 \rightarrow S_1$ energy is larger in the gas phase than in methanol). Changes in excitation maxima due to solvation

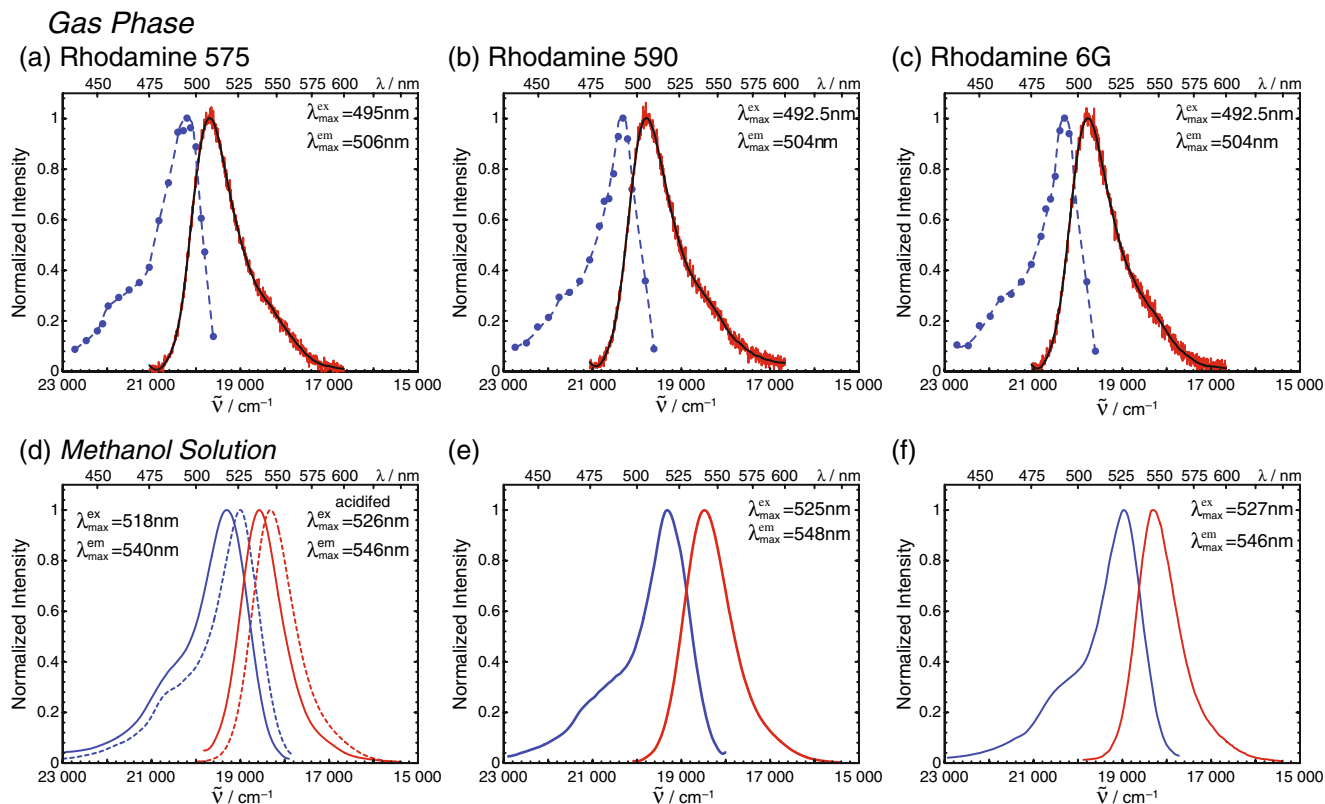


Figure 1. Fluorescence excitation (blue) and emission (red) spectra of (a),(d) R575, (b),(e) R590 and (c),(f) R6G measured in the gas phase (top) and in methanolic solution (bottom). Emission spectra were measured using 470 nm excitation. The excitation and emission maxima ($\lambda_{\text{max}}^{\text{ex}}$, $\lambda_{\text{max}}^{\text{em}}$) are indicated. There is a systematic bathochromic shift in both the excitation and emission maxima observed in transition from the gas phase to the condensed phase for each of these dyes. The measured fluorescence Stokes shifts are significantly larger in solution than in the gas phase

Table 3. A summary of the spectral features identified and estimated uncertainties^{a,b} for the three rhodamine dyes shown in Figure 1

	R575			R590		R6G	
	Gas phase	Methanol (R19 ⁺)	Acidified methanol (R19H ⁺)	Gas phase	Methanol	Gas phase	Methanol
$\lambda_{\max}^{\text{ex}}$ (nm)	495±2.5	518±1	526±1	492.5±2.5	525±1	492.5±2.5	527±1
$\lambda_{\max}^{\text{em}}$ (nm)	506±1	540±1	546±1	504±1	548±1	504±1	546±1
E_{FSS} (cm ⁻¹)	-440	-790	-700	-460	-800	-460	-660
$\Delta E_{0-1}^{\text{ex}}$ (cm ⁻¹)	+1500	+1300	+1600	+1300	+1150	+1300	+1200
$\Delta E_{0-1}^{\text{em}}$ (cm ⁻¹)	-1500	-	-	-1300	-	-1300	-

^aRelative uncertainties given for the solution-phase excitation and emission and gas-phase emission maxima are estimated to be approximately ±1 nm.

^bAbsolute uncertainties shown for the gas-phase excitation maxima are based on the wavelength interval between successive measurements of 2.5 nm.

(ΔE_s) are similar among the three dyes: -1190 cm⁻¹, -1260 cm⁻¹ and -1330 cm⁻¹ for R575, R590 and R6G, respectively. This observation is consistent with a picture in which the more highly polarizable excited state is preferentially stabilized with respect to the ground state by favorable interactions with the solvent [39].

R575

The excitation and emission maxima of R575 in acidified methanol ($\lambda_{\max}^{\text{ex}} = 526$ nm, $\lambda_{\max}^{\text{em}} = 546$ nm) agree reasonably well with those reported by Arbeloa et al. for R19H⁺ in acidified ethanol ($\lambda_{\max}^{\text{ex}} = 527.4$ nm, $\lambda_{\max}^{\text{em}} = 549.6$ nm) [44]. Of the three dyes investigated in this work, R575 has the smallest change in excitation energy upon transfer from the gas phase to methanolic solution (1190 cm⁻¹). The observed fluorescence Stokes shift (E_{FSS}) for gaseous R575 (-440 cm⁻¹) is approximately two-thirds that of R575 solvated in methanol (-700 cm⁻¹). This result indicates that there is a smaller change in molecular geometry from $S_0 \rightarrow S_1$ in the gas phase than in solution.

R590 and R6G

The excitation and emission profiles of R590 (Figure 1b) and R6G (Figure 1c) are essentially indistinguishable from each other in the gas phase. The identified maxima, $\lambda_{\max}^{\text{ex}} = 492.5$ nm and $\lambda_{\max}^{\text{em}} = 504$ nm, are the same within the uncertainty of the measurements (estimated to be ±1 nm relative uncertainty). In solution, R590 and R6G have similar, yet not identical, spectral properties. The excitation maxima are the same, while the emission maxima differ by 2 nm; the fluorescence Stokes shift is -800 cm⁻¹ for R590 but only -660 cm⁻¹ for R6G. These data indicate that despite the structural similarity between these two dyes, the solvated R590 system undergoes a more significant geometrical reorganization of the chromophore and surrounding solvent molecules in the excited state than does solvated R6G. This difference is not observed in the gas phase. Thus, the spectroscopic differences between R590 and R6G in methanol are a consequence of solvation and are not due to the intrinsic electronic properties of the two dyes. The

fluorescence Stokes shifts measured in the gas phase (-460 cm⁻¹) are approximately half (R590) to a third (R6G) compared to the Stokes shift in solution. These relatively small gas-phase Stokes shifts indicate that, much like R575, there is a high degree of similarity between the ground electronic state (S_0) and the excited electronic S_1 geometries for gaseous R590 and R6G.

Comparison with Computations

Table 4 summarizes measured and computed values for the $S_0 \rightarrow S_1$ transition for R6G and the associated change in transition energy due to solvation (ΔE_s). R6G exhibits mild solvatochromism, with ΔE_s between the gas phase and protic solvents ranging from -1290 to -1440 cm⁻¹.

Guthmuller and Champagne [51] reported electronic transition energies for R6G computed using time-dependent density functional theory (TD-DFT) at the B3LYP/6-311G* level of theory with a polarizable continuum model for solvent interaction. The vertical $S_0 \rightarrow S_1$ transition was computed to lie at 429 nm in vacuum and at 449 nm in ethanol. The predicted solvent shift of -1050 cm⁻¹ is in the same direction, though somewhat smaller than is found with experiment (-1440 cm⁻¹) [44, 46]. However, it is worth noting that the level of theory used significantly overestimates the measured $S_0 \rightarrow S_1$ transition energies both in the gas phase (by +3010 cm⁻¹) and in solution (by +3400 cm⁻¹). A simulated absorption spectrum of gaseous R6G from the same report [51] accurately predicts both the location ($\Delta E_{0-1} \approx +1300$ cm⁻¹) and the relative intensity ($I_{0-1} \approx 0.25$) of a vibronic shoulder [51] relative to the band origin, which is in excellent

Table 4. A summary of measured and computed values for the $S_0 \rightarrow S_1$ transition of R6G in vacuum and in several solvents. The changes in maximal transition energy due to solvation (ΔE_s) are also tabulated

	Theory		Experiment	
	$S_0 \rightarrow S_1$ (nm) [ref]	ΔE_s (cm ⁻¹)	$S_0 \rightarrow S_1$ (nm) [ref]	ΔE_s (cm ⁻¹)
In vacuo	473 [50] 429 [51]	-	492.5 (this work)	-
H ₂ O	508 [50]	-1450	526 [44, 46]	-1290
Methanol	-	-	527 [46], (this work)	-1330
Ethanol	449 [51]	-1050	530 [44, 46]	-1440

agreement with the measured fluorescence excitation spectrum ($\Delta E_{0-1} \approx +1300 \text{ cm}^{-1}$, $I_{0-1} \approx 0.28$) from this work, as shown in Figure 1c and summarized in Table 3.

Jensen et al. [50] also investigated R6G using TD-DFT computations employing the BP86 functional and the COSMO methodology to account for solvent. The $S_0 \rightarrow S_1$ transition *in vacuo* was computed to lie at 473 nm and in water at 508 nm. There is reasonable agreement between the $S_0 \rightarrow S_1$ computed in vacuum and the fluorescence excitation maximum measured here, which differ by just 830 cm^{-1} . Computations at this level of theory also slightly overestimate the magnitude of the solvent shift, which is computed to be -1450 cm^{-1} in water, compared to the experimental value of -1290 cm^{-1} .

Fluorescence Power Dependence

Emission spectra of gaseous R575, R590 and R6G were measured using excitation laser powers ranging from 0 to 30 mW. Figure 2 compares the power dependence of the integrated fluorescence intensity in the range 475–600 nm measured for all three dyes under the same experimental conditions (see Table 1). For this series of experiments, an excitation wavelength of 470 nm, which is well to the blue of each dye's excitation maximum, was used for two reasons. First, excitation at 470 nm allows observation of the high-energy side of the emission spectrum, which rises from $\sim 480 \text{ nm}$. The bandwidth of the visible laser light ($<10 \text{ nm}$ FWHM) and the 480 nm sharp-cutoff long-pass filter we had available determined the wavelength closest to $\lambda_{\text{max}}^{\text{ex}}$ that could be used. Second, the normalized excitation intensities at 470 nm (Figure 1a–c) are virtually identical (0.33(8), 0.34(3), and 0.34(1)) for R575, R590, and R6G, respectively. The similarity in the relative excitation intensities suggests that the relative fluorescence intensity measured at $\lambda_{\text{ex}}=470 \text{ nm}$ should be a useful measure of the relative brightness (the product of absorption cross-section and quantum yield) of each dye.

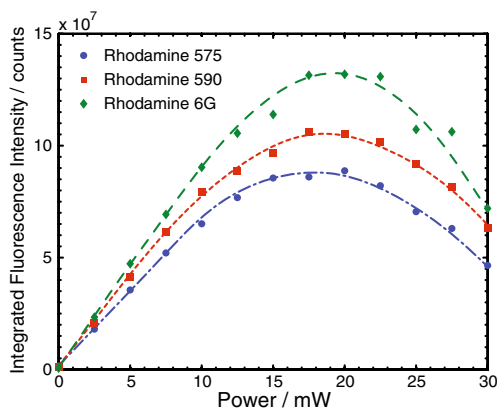


Figure 2. The integrated fluorescence intensities of R575, R590, and R6G with respect to laser power

The relative intrinsic brightnesses of these rhodamines in the gas phase are R575 (1.00) < R590 (1.15) < R6G (1.29) based on the measured integrated fluorescence intensities at the lowest laser power used ($P=2.5 \text{ mW}$). A similar ordering of gas-phase brightness for R575 and R6G was reported recently by Chingin et al. [20], who measured fluorescence from ions stored in an ICR cell using irradiation with the 488 nm line of an Ar-ion laser. Those authors reported that R6G appeared to be roughly twofold brighter than R575, and the disparity in fluorescence yield was ascribed to a difference in the absorption maxima between R575 and R6G (as one might infer from solution data measured at neutral pH). However, the excitation spectra shown in Figure 1a–c indicate that the normalized fluorescence excitation intensities of R575 and R6G at 490 nm (0.94 and 0.95, respectively) are essentially indistinguishable, so the observed difference in brightness cannot be explained by a shift in the absorption band. It is interesting to note that the relative brightness of R575 and R6G in the gas phase is opposite to the ordering expected based on the molar absorbance coefficients and fluorescence quantum yield in water and in ethanol reported by Arbeloa et al., which are 0.81 and 0.90, respectively [44].

The qualitative trend in fluorescence intensity with respect to laser power is similar for each dye shown in Figure 2. The measured fluorescence intensity rises linearly from zero power up to 7.5 mW, as expected. The slope of the R6G power dependence plot is greatest, while R575 is smallest, consistent with the relative brightnesses assigned above. Above 7.5 mW, each plot begins to show some curvature. The observed fluorescence intensity peaks between 17.5 and 20 mW for all three dyes and then drops off. The measured relative fluorescence intensities with respect to laser power are not constant. At its maximum, the fluorescence signal from R6G is 1.5 times that of R575 and 1.3 times that of R590. This is illustrated more clearly in Figure S-2 in the ESM, which shows plots of the integrated fluorescence intensities of R590 and R6G, normalized to the integrated intensity of R575, as a function of laser power. The relative fluorescence intensity of R6G ranges from 1.30 to 1.65 and that for R590 ranges from 1.15 to 1.35. The main cause of the decrease in measured fluorescence and change in relative fluorescence intensity with increasing laser power is photofragmentation, which is discussed in more detail below.

The emission profiles show small but clear changes with increasing laser power. This effect is shown in Figure 3, which displays the normalized fluorescence emission spectra measured at three different laser powers, processed with a first-order Savitzky–Golay digital filter. The emission profiles at every laser power measured are shown in the ESM (Figure S-4). Both a progressive redshift in the emission maxima ($\tilde{\nu}_{\text{max}}^{\text{em}}$) and a broadening of the emission spectra with increasing laser power are visible. A summary of the spectral features at high and low power is shown in Table S-1 and Figure S-4 of the ESM.

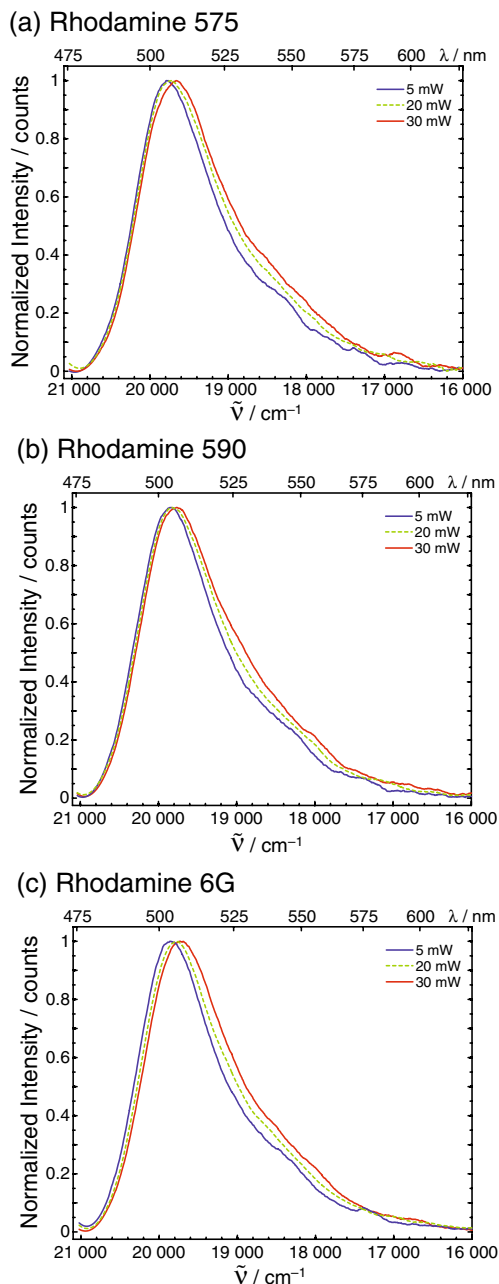


Figure 3. The effect of laser power on the emission spectra of (a) R575, (b) R590, and (c) R6G. Spectra were measured with $\lambda_{\text{ex}}=470$ nm, 5 s irradiation time, and laser powers of 5 mW (blue solid line), 20 mW (green dashed line) or 30 mW (red solid line)

The observed redshift of $\tilde{\nu}_{\text{max}}^{\text{em}}$ as excitation power is increased from 2.5 mW to 30 mW is small for all three dyes: -110 cm^{-1} for R575, -80 cm^{-1} for R590, and -130 cm^{-1} for R6G. The shift could result from two distinct phenomena: (1) progressive heating of the fluorescing ion population, and (2) emission from product ions. We will first discuss the photodissociation characteristics of the three dyes and an inves-

tigation of some of their important fragment ions before returning to the issue of the spectral redshifting and broadening.

Dissociation Mass Spectra

Figure 4 shows photodissociation mass spectra for (a) R575, (c) R590, and (e) R6G measured in the QIT. The photodissociation mass spectra were recorded with small ion populations to avoid space-charge effects and at $q_z=0.18$ to trap and detect low-mass fragment ions. Under conditions of high laser power (35 mW), the photodissociation spectra are rich, demonstrating numerous clusters of fragment ions in the mass range 150–400 Th. In addition to small neutral losses ($\cdot\text{CH}_3$, CH_4 , C_2H_4 , $\cdot\text{C}_2\text{H}_5$) that are observed first at lower laser powers, increasing the photon flux clearly allows access to high-energy, multiple-photon dissociation pathways that fragment the xanthen backbone of these ions.

The right hand side of Figure 4 shows high-resolution product ion spectra of the three dyes measured in a Fourier transform ion cyclotron resonance mass spectrometer (FT-ICR-MS) following CID in a hexapole collision cell. The extent of parent ion depletion is similar in all spectra ($\sim 90\%$ depletion), with the exception of the R6G CID spectrum (Figure 4f), in which the parent ion is $\sim 99\%$ depleted. In contrast to the “forest” of low-mass fragment ions produced by photodissociation, the smallest fragment ions observed in the CID spectra are all above m/z 250. While the majority of the product ion signals in the CID spectra can be accounted for by just a few fragment ions, there are in fact a large number of low-abundance fragment ions (see the ESM for a complete list of accurate masses and molecular formulae). The high mass-accuracy measurements indicate that there are significant contributions from fragment ions with both odd and even electron configurations. The three rhodamine dyes share many common CID fragment ions. The complex fragmentation patterns are shown with a Kendrick-style plot [52, 53] in Figure S-5 of the ESM. There are at least 30 fragment ions that are common to all three dyes, and there are more than 45 fragments of R575 and R6G that share the same molecular formulae. In contrast, there are at least 16 fragment ions that are unique to R590. The large number of common fragment ions is not altogether surprising, given the structural similarity of the three rhodamine dyes. These data suggest that R575 and R6G follow very similar dissociation pathways, while those of R590 are somewhat different.

Several product ions are observed with significantly higher intensity by CID than by photodissociation (Figure 4). The most conspicuous of these are m/z 399/401 (from R590), m/z 386 (from all three dyes), m/z 341 (primarily from R575 and R6G), and m/z 327 (from R590). These fragment ions all retain both nitrogens (see the tables of accurate masses in the ESM), suggesting that the xanthen backbone is preserved and that the fragment ions therefore might also have appreciable absorption cross-sections for visible light. To investigate this possibility, each of the fragment ions mentioned above was produced in the

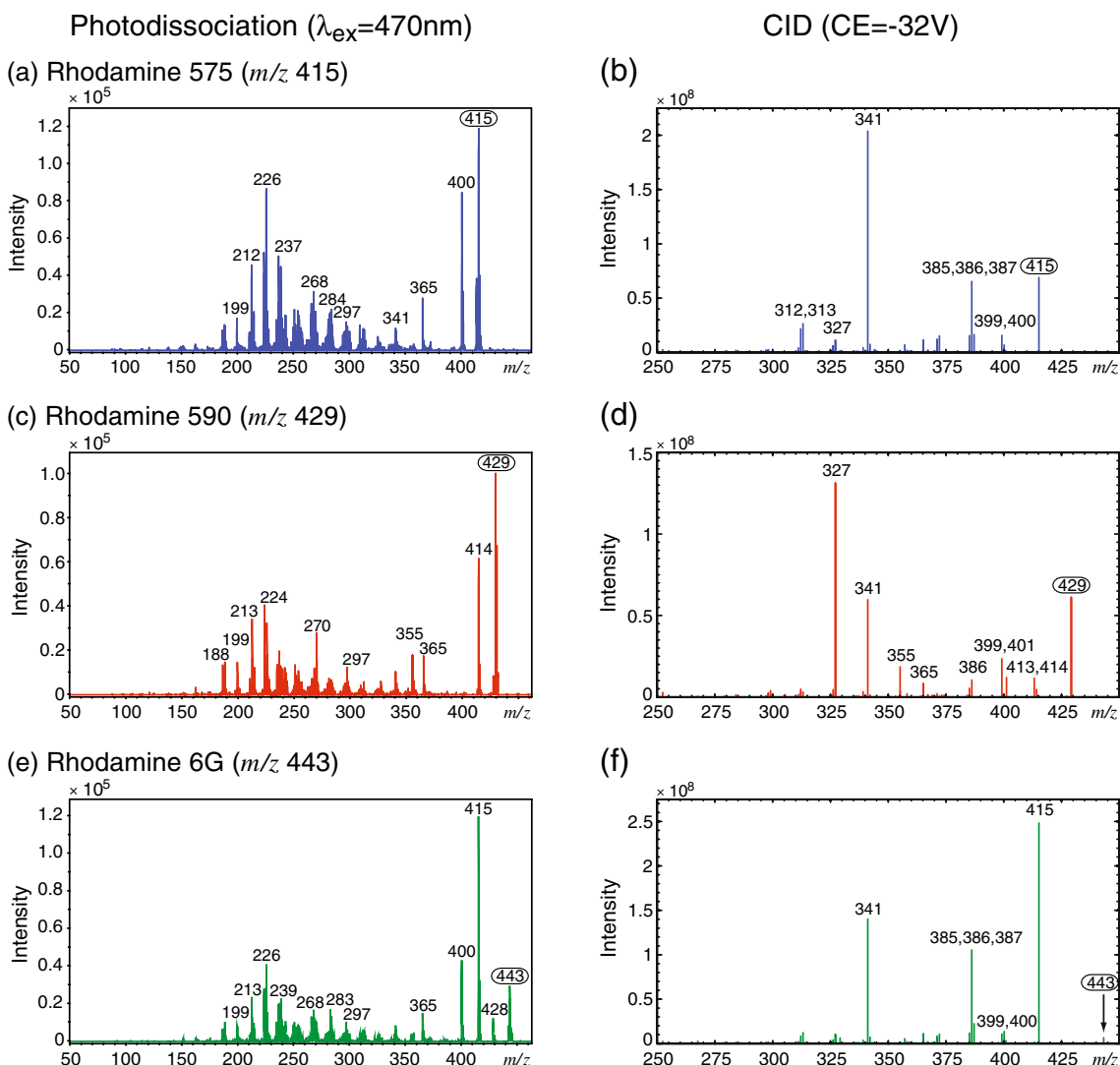


Figure 4. A comparison of the photodissociation (left: (a), (c), (e)) and collision-induced dissociation (right: (b), (d), (f)) product ion spectra of the three rhodamine dyes (R575: (a), (b); R590: (c), (d); R6G: (e), (f)). Photodissociation in the QIT was measured at $q_z=0.18$ to observe low-mass fragment ions with $\lambda_{\text{ex}}=470$ nm, $P=35$ mW, and $t_{\text{ex}}=3$ s. The accurate-mass CID spectra were measured in the FT-ICR-MS using mass selection of the precursor ion in the quadrupole, and following collisions with Ar in a hexapole collision cell. The laboratory collision energy was $\text{CE}=-32$ V. A table of accurate masses and assigned molecular formulae may be found in the ESM

quadrupole ion trap using CID, isolated, and irradiated with 470 nm light. Each product ion readily photodissociated. This suggests that populations of first-generation product ions that are observed with higher intensity in the CID spectra are depleted via secondary absorption/fragmentation in the PD mass spectra.

Photodissociation Power Dependence

Figure 5 shows the yield of remaining precursor and the sum of product ions for each dye, measured after the irradiation period, as a function of laser power. Error bars indicate one standard deviation from three replicate measurements. The photodissociation data were collected under the same

experimental conditions used for the fluorescence power dependence shown in Figure 2 ($q_z=0.6$, $P_{\text{He,trap}}=2.6 \times 10^{-3}$ mbar, $\lambda_{\text{ex}}=470$ nm, and $t=5$ s), with the exception of the size of the precursor ion population. Fluorescence was measured using large ion populations ($ICC \sim 1 \times 10^6$), and the photodissociation data were obtained from 30-fold lower “normal” ion populations for mass spectrometry ($ICC \sim 3 \times 10^4$). The highest fluorescence signal is observed using intermediate laser powers (17.5–20 mW, see Figure 2), at which the precursor ion population is depleted by ~ 75 – 80% at the end of the irradiation period.

The photodissociation breakdown plots show that there is a small amount of photodissociation, even at the lowest laser power of 2.5 mW. As power is increased, the *detected*

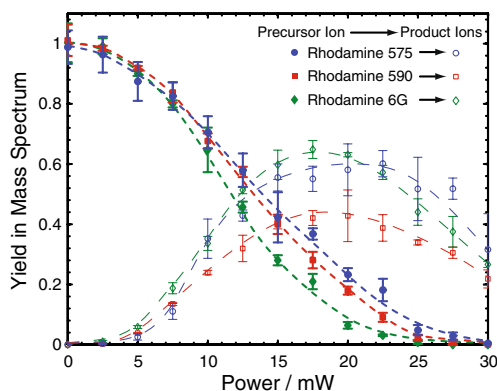


Figure 5. Precursor (solid symbols) and combined fragment (open symbols) ion yields for R575, R590, and R6G, computed according to Eqs. 1 and 2, and measured after irradiation with a range of laser powers

fragment ion yield increases, reaches a maximum, and then declines at the higher powers. It is important to note that the total ion current from precursor ions (prior to irradiation) is not recovered in the combined yield; if it was, the precursor and fragment ion yields after photoexcitation should sum to one. Clearly, some fragment ions are lost from the QIT due to the relatively high low-mass cutoff (LMCO) used for these experiments. Products ions with m/z values of less than 65% of the precursor ion mass are not stored in the trap and are not accounted for in the measured fragment ion current.

Interestingly, the order of relative gas-phase stability against photodissociation is $R575 > R590 > R6G$. Although the disappearance curves are quite similar, the remaining yield of the largest ion, R6G, declines the most sharply at low power, and R6G is completely dissociated beyond 25 mW. R590 yield declines less steeply with power, and a small fraction of m/z 429 remains up to 30 mW ($\sim 0.1\%$). Finally, the photodissociation yield of R575, the smallest ion, falls the least rapidly with respect to laser power. There is a noticeably higher yield remaining ($\sim 0.5\%$) at $P=30$ mW.

Figure 6 shows plots of the natural logarithm of the precursor ion yield as a function of laser power for the data sets shown in Figure 5. Error bars indicate one standard deviation from three replicate measurements. For a single-photon process, the decay of a precursor ion population is characterized by a single exponential decay such that a plot of $\ln(\text{yield})$ with respect to laser power is linear. Clearly, there is a nonlinear relationship with laser power in this experiment, indicating that photodissociation proceeds by the absorption of multiple photons. The data have been fitted with a fourth-order polynomial. Note that beyond $\ln(\text{yield}) = -4$, the remaining precursor ion abundance is less than 2%, resulting in large uncertainties.

The inset to Figure 6 shows plots of the unimolecular dissociation rate constants (assuming pseudo-first-order kinetics, computed using Eq. 3) as a function of the square of laser power (P^2) in the range of powers where the yield of remaining precursor ions is above 0.2. The computed rate

constants follow the order $k_{\text{diss}}^{R575} < k_{\text{diss}}^{R590} < k_{\text{diss}}^{R6G}$. Univariate linear regression models indicate that there is a convincing relationship ($r^2 > 0.992$) with P^2 in the low-power regime up to powers of 17.5, 20.0 and 22.5 mW for R6G, R590 and R575, respectively. However, this relationship breaks down at higher laser powers (see Figure S-3 in the ESM). The data here suggest that *with lower laser power*, the observed trend in the photodissociation yields of the three rhodamine dyes is consistent with a sequential two-photon model for dissociation [40, 41]. Note that the absorption of two photons from within the same pulse (multiphoton absorption) can be ruled out due to the low pulse energies (30 mW = 375 pJ/pulse) used here.

Ervin and coworkers [17, 38] have also examined photodissociation and fluorescence from R575 in a quadrupole ion trap. Using irradiation at 488 nm and several different pressures of He, dissociation rate constants were reported ranging from 0.2 s^{-1} (at 1.3×10^{-3} mbar) up to 35 s^{-1} (at 6.2×10^{-4} mbar) with laser powers spanning from 10 to 300 mW. The dissociation rate constants measured by Ervin's group [17] did not depend on the square of laser power. The dissociation rate constants measured in our work are lower, spanning from 0.02 s^{-1} up to 1.4 s^{-1} . The difference in observed power dependence must be due to the relative excitation and cooling rates in the two experiments.

Fluorescence from Fragment Ions

One potential source of difficulty in trapping MS experiments is that fragment ions formed via photodissociation (and whose structures are not altered significantly) might subsequently absorb photons and contribute additional

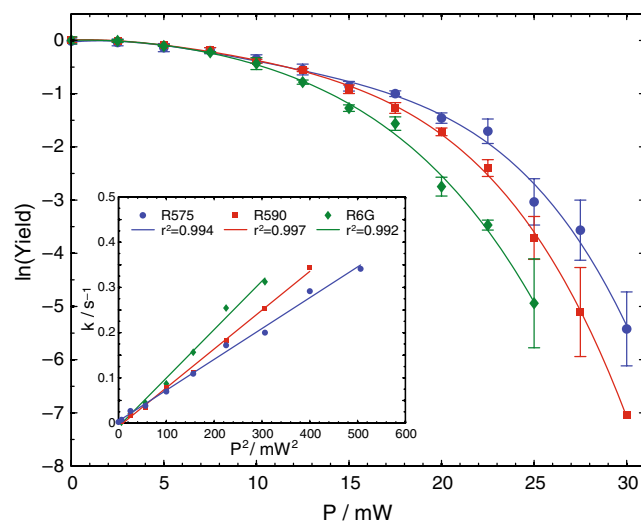


Figure 6. Plots of $\ln(\text{yield})$ of the precursor ions (R575, R590, and R6G) as a function of laser power. The experimental data are fitted with a fourth-order polynomial. *Inset:* plots of the dissociation rate constant (k_{diss}) as a function of the square of the laser power (P^2) for powers at which 20% or more of the parent ions remain after irradiation, fitted with univariate linear regression

fluorescence to the measured signal [2, 4, 12, 17, 20]. The emission spectra shown in Figure 1 were measured at low irradiation power to avoid contributions from any such photofragments. To investigate the effect of fragment ions on measured emission spectra, the optical characteristics of several fragment ions were investigated using MS³ in the quadrupole ion trap. All of the significant CID fragment ions (Figure 4, right hand side) that are observed to a lesser extent in the photodissociation spectra (Figure 4, left hand side) absorb 470 nm light and can be photodissociated in the QIT (data not shown). In each case, these ions are significantly more difficult to photodissociate than their respective precursor ions, requiring much higher laser powers to achieve a given fragmentation yield. This could be due to lower absorption cross-sections at 470 nm or it may simply indicate higher thresholds to photodissociation. Of these, only a few show appreciable fluorescence yields. These are discussed below.

m/z 415

Perhaps the most interesting fragment ion in this group of structurally similar dyes is that with an *m/z* value of 415, which was addressed briefly by Chingin et al. [20]. The *m/z* 415 ion (C₂₆H₂₇N₂O₃⁺) is the R575 precursor, but it is also the most intense fragment of the ethyl ester R6G. Resulting from the loss of ethene, *m/z* 415 is observed in both the photodissociation and CID spectra of R6G. In fact, with the exception of *m/z* 428 (loss of ·CH₃ from R6G), the product ions observed in the photodissociation spectra of R6G and R575 are virtually identical, as are the CID spectra (see also Figure S-5 in the ESM). These results support Chingin's proposal that the fragmentation of gaseous R6G is initiated predominantly via the loss of C₂H₄ from the ethyl benzoate [20], and Schmidt and Penzkofer's observations from powdered samples [54].

The results of an MS³ fluorescence experiment on the *m/z* 415 fragment ion are shown in Figure 7a. The *m/z* 415 fragment ion was produced by CID of R6G (*m/z* 443) in the QIT, isolated and cooled for a period of 1 s. Subsequently, the cooled population was irradiated with 470 nm light for 5 s. The fluorescence emission spectrum of the R6G→*m/z* 415 product ion was processed with a first-order Savitzky–Golay digital filter, and is the red trace shown in Figure 7a. A fluorescence emission spectrum of the same number of R575 ions (smoothed blue trace) was subsequently measured under the same experimental conditions. The intensities, band profiles, and emission maxima of these two spectra are the same within the uncertainty of the measurement. These results confirm that the *m/z* 415 product ion formed via the dissociation of R6G is spectroscopically identical to R575.

R590→*m/z* 414

Another interesting fragment ion observed in the photodissociation spectrum (Figure 4b) is that with an *m/z* value of 414, formed by the loss of ·CH₃ from R590 (*m/z* 429).

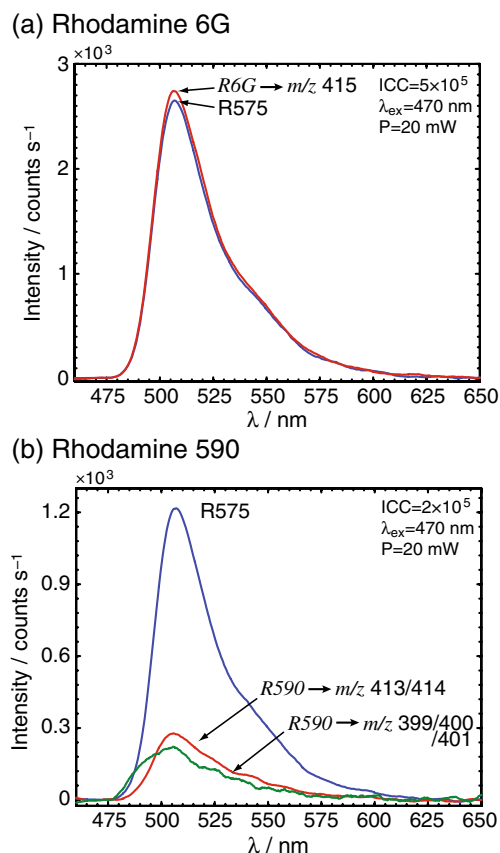


Figure 7. Smoothed MS³ fluorescence emission spectra of fragment ions from (a) R6G and (b) R590. Fragment ions were produced by collision-induced dissociation in the QIT, isolated and irradiated with 470 nm light. In each plot, a reference spectrum from R575 obtained under identical experimental conditions ($P=20$ mW, ICC , $t_{ex}=5$ s) is included for comparison

The MS³ fluorescence spectrum of R590→*m/z* 414 (red trace) is shown in Figure 7b, along with a reference spectrum of R575 (blue trace, $\lambda_{max}^{em} = 507$ nm). The relative intensity of the emission from *m/z* 414 is approximately fourfold lower than that from R575, and the emission maximum appears at the same position as that of the R590 precursor ion ($\lambda_{max}^{em} = 505$ nm). Only a small population of *m/z* 414 could be isolated ($ICC \sim 2 \times 10^5$). The low fluorescence yield of *m/z* 414 compared to R575 makes it unlikely that this fragment ion contributes much fluorescence to the emission spectra of R590 measured at low laser powers, where this fragment ion is in low abundance.

m/z 399/400/401

We have also investigated the group of fragment ions corresponding to the cluster at *m/z* 399, 400 and 401. *m/z* 400 is observed in the photodissociation spectra of both R575 and R6G, but is notably absent from the spectrum of R590 measured at 35 mW laser power (Figure 4c). At lower laser powers (not shown), the *m/z* 400 fragment from R590

is observed, and this accounts for 50% of the fragment ion abundance with 5 mW excitation. Thus, the m/z 400 fragment ion from R590 appears to photodissociate more readily than that from R6G or R575. The high-resolution CID data (see also the ESM) provides some additional information: (1) m/z 400.1781 has the same molecular formula ($C_{25}H_{24}N_2O_3^+$) in each of the CID spectra from R575, R590, and R6G; (2) an additional fragment ion with an m/z value of 399.1703 ($C_{25}H_{23}N_2O_3^+$) also appears in each of the CID spectra; (3) there is a unique fragment ion with an m/z value of 401.1860 ($C_{25}H_{25}N_2O_3^+$) that is observed from CID of R590 but not R6G or R575. The ions with m/z 399 or 401 are not significant photodissociation fragments ($\leq 1\%$ yield) at any power. A small fluorescence signal was measured from the m/z 399, 400, 401 ensemble created by CID of R590. This is shown in Figure 7b. In contrast, no gas-phase fluorescence emission was observed for these fragment ions from either R575 or R6G (data not shown).

The measured emission spectrum of R590 \rightarrow m/z 399/400/401 has a markedly different band profile than the R575 reference. There is a weakly defined maximum at approximately 505 nm that is similar to the R590 precursor, but the emission band also exhibits a feature below 500 nm that is cut off by the 480 nm filter, quite different from the other emission spectra shown in this work. At this time, we have not pursued further emission measurements using a different filter set and a shorter wavelength excitation, since the relative intensity of the observed emission (passing the 480 nm long-pass filter) is approximately fivefold lower than the reference R575.

Of all the fragment ions investigated here, only m/z 415 from R6G and to a lesser extent fragments from R590 show fluorescence signals that are sufficiently high to contribute significantly to the emission spectra obtained under the low-power conditions shown in Figure 1. We can be confident from the measured photodissociation yield of the m/z 415 from R6G at 5 mW ($Y_{415}=0.025$) that any contribution from this fragment ion does not contribute significantly to the measured emission profile. However, the photodissociation yields of m/z 415 (from R6G), m/z 414 (from R590) and m/z 399/400/401 (also from R590) are not insignificant at high laser power. A portion of the observed redshift for R6G upon irradiation at high laser power can be attributed to the presence of m/z 415, which has an emission maximum that is approximately 2.5 nm to the red of R6G. However, neither R575 nor R590 have brightly fluorescent fragments that are to the red of their respective parent ions, ruling the fluorescence of fragment ion(s) out as a source of the redshifts observed from these ions.

Photoactivation/Deactivation Cycle

The emerging picture for the photoactivation/deactivation of the three rhodamine dyes in the quadrupole ion trap points to a sequential, multiple-photon dissociation mech-

anism with multiple excitation/emission cycles. Previous investigations of xanthene dyes in quadrupole ion traps [2, 4, 12, 17, 38] have highlighted the observed pressure dependence of the photodissociation rate constant (k_{diss}), which is expected for multiple-photon activation [55]. A plot of $\ln(\text{yield})$ of the precursor ion with respect to irradiation power (Figure 6) shows a higher order relationship that is consistent with multiple-photon activation. At low irradiation power, k_{diss} depends quadratically on laser power. This suggests a two-photon mechanism for dissociation, although at higher laser powers this relationship breaks down.

In a similar investigation of photodissociation of R575 in a quadrupole ion trap, Ervin and coworkers [17, 38] also found that a simple two-photon model was insufficient to describe their data. The authors first proposed a termolecular model [38] invoking two distinct excited states, three distinct absorption cross-sections, and two separate termolecular relaxation rate constants to fit the experimental data. In a later publication that included the direct observation of fluorescence from R575, a three-state model was proposed in which an intermediate (such as a long-lived triplet state) provides a doorway state that was said to be required for photodissociation [17]. In the same article, Ervin's group also pointed out that sequential absorption–emission through a Franck–Condon walking mechanism might also explain the observed photodissociation.

The spectroscopic data and dissociation kinetics presented here point to a model that allows for *both* absorption/emission cycling as well as a two-photon mechanism for photodissociation. Figure 8 shows a schematic energy level diagram describing two models for the activation, emission, collisional cooling and photodissociation of rhodamine dyes in the quadrupole ion trap. Four states are shown: the ground electronic state (S_0), the first electronic state (S_1), a triplet state (T_1), and a hypothetical dissociative state (D_S) characterized by some threshold energy for photodissociation. Representative vibrational energy levels of S_0 , S_1 and T_1 are indicated. M^+ refers to the ion in its electronic ground state, while M^{+*} and $M^{+*\dagger}$ refer to the ion in a singlet or triplet electronic state, respectively. $M^+[v^*]$ refers to a vibrationally excited ion in the ground electronic state, while N and P^+ are the neutral and product ions following photodissociation, respectively. Electronic transitions are shown as follows: resonant absorption of a photon ($h\nu_A$, blue arrows), fluorescence emission ($h\nu_E$, green arrows), internal conversion (k_{IC}) and intersystem crossing (k_{ISC} , wavy black arrows). In each step, absorption is followed rapidly by either vibrational relaxation (k_{VR} , wavy red arrows) or photodissociation (k_D and k_D' , red arrows). Vibrational relaxation within the ground electronic state via multiple collisions with helium and infrared emission are represented by the short black arrows. Finally, a cartoon representing the distribution of populated vibrational levels is represented by the symbol $N(E)$, and is intended to show *qualitatively* the progression of the internal energy distribution of the ion ensemble.

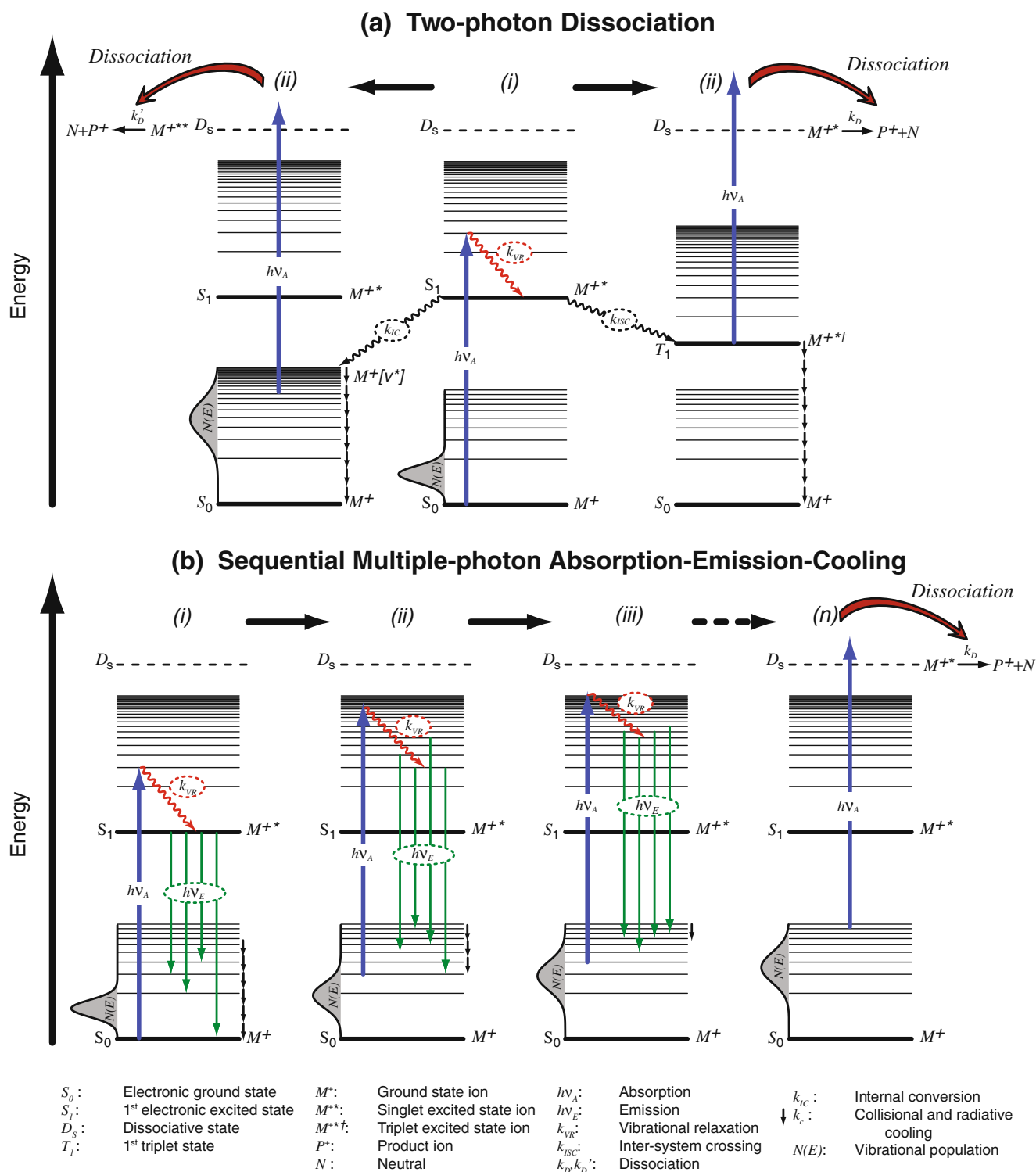


Figure 8. A schematic energy level diagram illustrating the absorption–emission cycle with two possible routes to photodissociation: (a) a two-photon mechanism, and (b) a model for sequential absorption–emission–collisional cooling

In broad terms, the diagram summarizes two possible routes to photodissociation, either through sequential two-photon dissociation (route A), or through multiple, sequential absorption/emission cycling leading to slow vibrational heating (route B). In the two-photon model, following the

absorption of a first photon, the ground state ion M^+ is elevated to the first electronic excited state and can undergo either intersystem crossing to a long-lived triplet state ($M^{*+\ddagger}$, right-hand side), as explored by Kappes and coworkers [56], or internal conversion to a vibrationally

excited level of the electronic ground state ($M^+[v^*]$, left-hand side). It is not surprising that nonradiative relaxation channels are available even to these highly fluorescent dyes. They all have quantum yields of <1 in solution; values of 0.77 [44] and 0.95 [45, 46] have been reported for R6G. Radiative decay rates of R19H⁺ (R575) and R6G in ethanol were reported to be $k_r=2.16$ and $2.00 \times 10^8 \text{ s}^{-1}$, and nonradiative decay constants $k_{nr}=0.47$ and $0.60 \times 10^8 \text{ s}^{-1}$ were noted, respectively [44]. Clearly, there are appreciable rates of nonradiative decay from S_1 . In the two-photon model, the measured rate of photodissociation (i.e., the disappearance of M^+) depends on the rate of internal conversion populating the $M^+[v']$ states, and on the relative rates of absorption of a second photon (which depends on the rate of photon fluence, the absorption cross-section of the intermediate $M^+[v']$), and collisional cooling. If the rate of two-photon absorption exceeds (sufficiently) the rate of collisional cooling, absorption of the second photon can lead directly to photodissociation for the fraction of the ion population with enough excess internal energy to surpass the dissociation threshold. Higher rates of collisional cooling allow faster recovery of the ground state before the absorption of a second photon, and hence the observed rate of dissociation is reduced.

Route B illustrates sequential absorption/emission cycles that slowly pump up the internal energy of the ion. Multiple cycles of absorption and emission will naturally lead to a buildup of vibrational energy as a direct consequence of the fluorescence Stokes shift. For example, consider the emission spectrum of R575 shown in Figure 1a, obtained using irradiation at $\lambda_{\text{ex}}=470 \text{ nm}$ ($21,280 \text{ cm}^{-1}$). The weighted-average Stokes shift between $\lambda_{\text{em}}=480$ and 600 nm ($20,830 \text{ cm}^{-1}$ and $16,670 \text{ cm}^{-1}$, respectively) is nearly 2000 cm^{-1} (0.25 eV). Without collisional cooling or substantial infrared radiative emission, significant vibrational energy is therefore accumulated through just a few absorption/emission cycles. The rate of photodissociation through this pathway will be governed by the relative rates of pumping via absorption (laser power, absorption cross-section), the rate of internal energy buildup (magnitude of the Stokes shift), and the combined rates of deactivation via emission (fluorescence quantum yield and infrared radiative emission rates) and collisional cooling (pressure). It has been pointed out previously [4, 17] that the time-frame for fluorescence ($\sim 10 \text{ ns}$) is as much as 3–4 orders of magnitude faster than the rate of collisions ($\sim 1\text{--}50 \text{ }\mu\text{s}$) at the pressures in the QIT ($\sim 1\text{--}3 \times 10^{-3} \text{ mbar}$). Nevertheless, the fluorescence signal from gas-phase ions shows a strong pressure dependence [2, 4, 12, 19, 20]. Higher rates of collisional cooling allow for more absorption/emission cycles before reaching the photodissociation threshold through this pathway.

The appearance of the fluorescence emission spectra with respect to laser power (redshift and broadening shown in Figure 3) is strong evidence of fluorescence from a heated ion population. Under experimental conditions in which the rate of collisional cooling is constant (i.e., at constant

pressure), increasing the photon flux also increases the probability of an ion absorbing an additional photon before the initial internal energy distribution is recovered. Consequently, absorption of an additional photon can occur from a higher vibrational level of S_0 , thereby populating higher vibrational levels of S_1 . The broadening and redshifting of the emission spectrum is consistent with fluorescence transitions occurring from vibrationally excited levels of S_1 . In summary, *route A* provides an explanation for the two-photon power dependence shown at lower laser powers (Figure 6, inset). Cycling of excitation and emission through *route B* provides a gradual heating mechanism, consistent with the observed spectral changes at higher excitation powers, which could also explain the overall higher order power dependence (Figure 6).

Conclusions

The laser-induced fluorescence excitation, emission, and photodissociation characteristics of three structurally similar rhodamine dyes (rhodamine 575, rhodamine 590, and rhodamine 6G) have been investigated in a modified quadrupole ion trap mass spectrometer. Dispersed fluorescence spectra were obtained using excitation at $\lambda_{\text{ex}}=470 \text{ nm}$ with low laser power ($P=4 \text{ mW}$) to minimize photodissociation and vibrational heating of the precursor ion population. The measured excitation and emission maxima are: $\lambda_{\text{max}}^{\text{ex}} = (495 \pm 2.5) \text{ nm}$ and $\lambda_{\text{max}}^{\text{em}} = (506 \pm 1) \text{ nm}$ for R575; $\lambda_{\text{max}}^{\text{ex}} = (492.5 \pm 2.5) \text{ nm}$ and $\lambda_{\text{max}}^{\text{em}} = (504 \pm 1) \text{ nm}$ for R590; and $\lambda_{\text{max}}^{\text{ex}} = (492.5 \pm 2.5) \text{ nm}$ and $\lambda_{\text{max}}^{\text{em}} = (504 \pm 1) \text{ nm}$ for R6G. These results show that the excitation and emission spectra of R590 and R6G are essentially indistinguishable in the gas phase, and that R575 is also very similar. The results have been compared with previously published results from ab initio computations.

For all three protonated dyes, solvation in methanol gives rise to significant shifts in excitation energy, ranging from $\Delta E_s = -900 \text{ cm}^{-1}$ for R575 to -1260 cm^{-1} for R590 and to -1330 cm^{-1} for R6G. These results indicate that solvation in methanol preferentially stabilizes the excited state in the condensed phase compared to stabilization provided to the ground state. The fluorescence Stokes shifts are also significantly larger in methanol than in the gas phase, increasing from 440 cm^{-1} to 790 cm^{-1} for R575, from 460 cm^{-1} to 800 cm^{-1} for R590, and from 460 cm^{-1} to 660 cm^{-1} for R6G. The smaller Stokes shifts in the gas phase indicate that the conformational changes between S_0 and S_1 are smaller in the gas phase than in solution.

Laser power affects both the fluorescence and photodissociation yield. The increased absorption rates due to higher laser powers naturally increase the integrated fluorescence intensity, but beyond a certain power, depletion of the precursor ion population via photodissociation causes a decline in the fluorescence signal. Based on the measured photodissociation yields, the order of relative gas-phase photostability is R575 > R590 > R6G. In contrast, the order of

apparent “brightness” is R575 (1) < R590 (1.15) < R6G (1.29).

A small bathochromic shift in the measured emission maxima is observed as a function of laser power. The measured shift is -110 cm^{-1} for R575, -80 cm^{-1} for R590, and -130 cm^{-1} for R6G. Two possible causes for the observed shift were considered. First, the possibility of fluorescent fragments ions was explored; for R6G a significant fragment ion ($\text{R6G} \rightarrow m/z\ 415$) with mass and spectroscopic properties that are identical to R575 ($\Delta\tilde{\nu}_{\text{max}}^{\text{em}} = -70\text{ cm}^{-1}$ compared to R6G) contributes fluorescence at higher laser power. Emission from this fragment ion could explain in part the overall redshift ($\Delta\tilde{\nu}_{\text{max}}^{\text{em}} = -130\text{ cm}^{-1}$) observed for R6G. However, the presence of this fragment alone cannot account for the magnitude of the redshift for R6G. Moreover, no fluorescent fragment ions were identified from R575. Finally, while fluorescent fragment ions from R590 were identified, they are much less bright than the R590 precursor and are not significantly shifted to the red.

The observed redshift in fluorescence may also result from progressive heating of the precursor ion population. The emission spectra also show a systematic broadening with higher laser powers that is consistent with this picture. Multiple absorption/emission cycles over a long period of irradiation lead to an increase in the ion's residual vibrational energy as a result of the fluorescence Stokes shift. Unfortunately, it is difficult to estimate the number of fluorescence cycles a given ion experiences because the primary mode of ion heating most likely occurs through the interruption of the fluorescence cycle via internal conversion. The observed rate of photodissociation depends on not only the dissociation threshold but also the rate of photon fluence, the fluorescence quantum yield, the rate of collisional cooling, and the absorption cross-section of the intermediate state(s).

This report provides fundamental knowledge of the photophysical properties of three rhodamine dyes. Simultaneous observation of dispersed fluorescence and photodissociation improves our current understanding of the dynamics of photoactivation and deactivation in the quadrupole ion trap mass spectrometer. Fundamental studies such as these will be useful for implementing fluorescence energy transfer techniques such as FRET in order to investigate the conformations of gaseous ions.

Acknowledgements

The authors are grateful to the following sources for funding: the Natural Sciences and Engineering Research Council (NSERC), the Canada Research Chairs program, Canada Foundation for Innovation (CFI), the Government of Ontario, and the Estate of Margery Warren.

References

1. Jockusch, R.A., Bian, Q., Talbot, F.O., Forbes, M.W.: Development and characterization of laser induced fluorescence spectroscopy coupled

- with ion trap mass spectrometry Proc. 56th ASMS Conf. *Mass. Spectrom. Allied Topics*, Denver, CO, USA (2008)
2. Forbes, M.W., Talbot, F., Jockusch, R.A.: In: March, R.E., Todd, J.F.J. (eds.) Practical aspects of trapped ion mass spectrometry, vol. 5: applications of ion trapping devices. CRC Press, Boca Raton (2009)
3. Forbes, M.W., Jockusch, R.A.: Deactivation pathways of an isolated green fluorescent protein model chromophore studied by electronic action spectroscopy. *J. Am. Chem. Soc.* **131**, 17038–17039 (2009)
4. Bian, Q., Forbes, M.W., Talbot, F.O., Jockusch, R.A.: Gas-phase fluorescence excitation and emission spectroscopy of mass-selected trapped molecular ions. *Phys. Chem. Chem. Phys.* **12**, 2590–2598 (2010)
5. Khoury, J.T., Rodriguez-Cruz, S.E., Parks, J.H.: Pulsed fluorescence measurements of trapped molecular ions with zero background detection. *J. Am. Soc. Mass. Spectrom.* **13**, 696–708 (2002)
6. Danell, A.S., Parks, J.H.: FRET measurements of trapped oligonucleotide duplexes. *Int. J. Mass Spectrom.* **229**, 35–45 (2003)
7. Iavarone, A.T., Parks, J.H.: Conformational change in unsolvated trp-cage protein probed by fluorescence. *J. Am. Chem. Soc.* **127**, 8606–8607 (2005)
8. Iavarone, A.T., Duft, D., Parks, J.H.: Shedding light on biomolecule conformational dynamics using fluorescence measurements of trapped ions. *J. Phys. Chem. A* **110**, 12714–12727 (2006)
9. Iavarone, A.T., Meinen, J., Schulze, S., Parks, J.H.: Fluorescence probe of polypeptide conformational dynamics in gas phase and in solution. *Int. J. Mass Spectrom.* **253**, 172–180 (2006)
10. Iavarone, A.T., Patriksson, A., van der Spoel, D., Parks, J.H.: Fluorescence probe of Trp-cage protein conformation in solution and in gas phase. *J. Am. Chem. Soc.* **129**, 6726–6735 (2007)
11. Shi, X., Duft, D., Parks, J.H.: Fluorescence quenching induced by conformational fluctuations in unsolvated polypeptides. *J. Phys. Chem. B* **112**, 12801–12815 (2008)
12. Wright, K.C., Blades, M.W.: Fluorescence emission spectroscopy of trapped molecular ions. Proc. 51st ASMS Conf. *Mass. Spectrom. Allied Topics*, Montreal, Canada (2003)
13. Cai, Y., Peng, W.P., Kuo, S.J., Lee, Y.T., Chang, H.C.: Single-particle mass spectrometry of polystyrene microspheres and diamond nanocrystals. *Anal. Chem.* **74**, 232–238 (2002)
14. Peng, W.P., Cai, Y., Chang, H.C.: Optical detection methods for mass spectrometry of macroions. *Mass. Spectrom. Rev.* **23**, 443–465 (2004)
15. Peng, W.P., Cai, Y., Lee, Y.T., Chang, H.C.: Laser-induced fluorescence/ion trap as a detector for mass spectrometric analysis of nanoparticles. *Int. J. Mass Spectrom.* **229**, 67–76 (2003)
16. Cai, Y., Peng, W.P., Kuo, S.J., Sabu, S., Han, C.C., Chang, H.C.: Optical detection and charge-state analysis of MALDI-generated particles with molecular masses larger than 5 MDa. *Anal. Chem.* **74**, 4434–4440 (2002)
17. Sassin, N.A., Everhart, S.C., Dangi, B.B., Ervin, K.M., Cline, J.I.: Fluorescence and photodissociation of rhodamine 575 cations in a quadrupole ion trap. *J. Am. Soc. Mass. Spectrom.* **20**, 96–104 (2009)
18. Frankevich, V., Guan, X.W., Dashtiev, M., Zenobi, R.: Laser-induced fluorescence of trapped gas-phase molecular ions generated by internal-source matrix-assisted laser desorption/ionization in a Fourier transform ion cyclotron resonance mass spectrometer. *Eur. J. Mass Spectrom.* **11**, 475–482 (2005)
19. Dashtiev, M., Zenobi, R.: Effect of buffer gas on the fluorescence yield of trapped gas-phase ions. *J. Am. Soc. Mass. Spectrom.* **17**, 855–858 (2006)
20. Chingin, K., Chen, H., Gamez, G., Zenobi, R.: Exploring fluorescence and fragmentation of ions produced by electrospray ionization in ultrahigh vacuum. *J. Am. Soc. Mass. Spectrom.* **20**, 1731–1738 (2009)
21. Wang, Y., Hendrickson, C.L., Marshall, A.G.: Direct optical spectroscopy of gas-phase molecular ions trapped and mass-selected by ion cyclotron resonance: laser-induced fluorescence excitation spectrum of hexafluorobenzene (C_6F_6^+). *Chem. Phys. Lett.* **334**, 69–75 (2001)
22. Cage, B., Friedrich, J., Little, R.B., Wang, Y.S., McFarland, M.A., Hendrickson, C.L., Dalal, N., Marshall, A.G.: Wavelength resolved laser-induced fluorescence emission of $\text{C}_6\text{F}_3\text{H}_3^+$ trapped in an ion cyclotron resonance cell. *Chem. Phys. Lett.* **394**, 188–193 (2004)
23. Scott, J.R., Ham, J.E., Durham, B., Tremblay, P.L.: Ruthenium trisbipyridine as a candidate for gas-phase spectroscopic studies in a Fourier transform mass spectrometer. *Spectrosc. Int. J.* **18**, 387–396 (2004)
24. Friedrich, J., Fu, J.M., Hendrickson, C.L., Marshall, A.G., Wang, Y.S.: Time resolved laser-induced fluorescence of electrosprayed ions confined in a linear quadrupole trap. *Rev. Sci. Instrum.* **75**, 4511–4515 (2004)
25. Dashtiev, M., Azov, V., Frankevich, V., Scharfenberg, L., Zenobi, R.: Clear evidence of fluorescence resonance energy transfer in gas-phase ions. *J. Am. Soc. Mass. Spectrom.* **16**, 1481–1487 (2005)

26. Förster, T.: Intermolecular energy migration and fluorescence (translation). American Institute of Physics, New York, NY (1993)
27. Förster, T.: Zwischenmolekulare Energiewanderung und Fluoreszenz. *Ann. Phys.* **2**, 55–75 (1948)
28. Wuerker, R.F., Shelton, H., Langmuir, R.V.: Electrodynamic containment of charged particles. *J. Appl. Phys.* **30**, 342–349 (1959)
29. Neuhauser, W., Hohenstatt, M., Toschek, P., Dehmelt, H.: Optical-sideband cooling of visible atom cloud confined in parabolic well. *Phys. Rev. Lett.* **41**, 233–236 (1978)
30. Neuhauser, W., Forster, G., Toschek, P.E., Dehmelt, H.: Visual detection of electrostatically stored ions. *J. Opt. Soc. Am.* **68**, 623–623 (1978)
31. Schneider, R., Werth, G.: Ion storage technique for very long living states—decay-rate of the $^5D_{3/2}$ state of Ba-II. *Z. Phys. A: Hadrons Nucl.* **293**, 103–106 (1979)
32. Werth, G.: Optical spectroscopy in ion traps. *Eur. Phys. J. D.* **45**, 121–124 (2007)
33. Werth, G.: Ion traps and their application in spectroscopy. *Hyperfine Interact.* **99**, 3–30 (1996)
34. Leibfried, D., Blatt, R., Monroe, C., Wineland, D.: Quantum dynamics of single trapped ions. *Rev. Mod. Phys.* **75**, 281–324 (2003)
35. Razvi, M.A.N., Chu, X.Z., Alheit, R., Werth, G., Blumel, R.: Fractional frequency collective parametric resonances of an ion cloud in a Paul trap. *Phys. Rev. A.* **58**, R34–R37 (1998)
36. Green, M., Wodin, J., Devoe, R., Fierlinger, P., Flatt, B., Gratta, G., LePort, F., Diez, M.M., Neilson, R., O’Sullivan, K., Pocar, A., Waldman, S., Leonard, D.S., Piepke, A., Hargrove, C., Sinclair, D., Strickland, V., Fairbank, W., Hall, K., Mong, B., Moe, M., Farine, J., Hallman, D., Virtue, C., Baussan, E., Martin, Y., Schenker, D., Vuilleumier, J., Vuilleumier, J., Weber, P., Breidenbach, M., Conley, R., Hall, C., Hodgson, J., Mackay, D., Odian, A., Prescott, C.Y., Rowson, P.C., Skarpaas, K., Wamba, K.: Observation of single collisionally cooled trapped ions in a buffer gas. *Phys. Rev. A.* **76**, 023404 (2007)
37. Enders, K., Stachowska, E., Marx, G., Zolch, C., Georg, U., Dembczynski, J., Werth, G.: Ground-state hyperfine-structure measurements of unstable Eu^+ isotopes in a Paul ion trap. *Phys. Rev. A.* **56**, 265–269 (1997)
38. Sassin, N.A., Everhart, S.C., Cline, J.I., Ervin, K.M.: Photodissociation and collisional cooling of rhodamine 575 cations in a quadrupole ion trap. *J. Chem. Phys.* **128**, 234305 (2008)
39. Lakowicz, J.: Principles of fluorescence spectroscopy, 3rd edn. Springer, New York, NY (2006)
40. Freiser, B.S., Beauchamp, J.L.: Laser photodissociation of benzene radical cations—evidence for a two photon process involving long lived intermediate. *Chem. Phys. Lett.* **35**, 35–40 (1975)
41. Dunbar, R.C., Fu, E.W.: Ion photodissociation in the two-photon region. Spectroscopy and collisional quenching of bromobenzene cations. *J. Phys. Chem.* **81**, 1531–1536 (1977)
42. van Velzen, P., Van der Hart, W.J.: An Icr study of sequential two-photon dissociation of benzene, cyanobenzene and bromobenzene molecular ions. *Chem. Phys.* **61**, 325–334 (1981)
43. van der Hart, W.: Photodissociation of trapped ions. *Mass. Spectrom. Rev.* **8**, 237–268 (1989)
44. Arbeloa, F.L., Arbeloa, T.L., Lage, E.G., Arbeloa, I.L., Deschryver, F. C.: Photophysical properties of rhodamines with monoethylamino groups R19 and R6G in water–ethanol mixtures. *J. Photochem. Photobiol. A* **56**, 313–321 (1991)
45. Kubin, R.F., Fletcher, A.N.: Fluorescence quantum yields of some rhodamine dyes. *J. Lumin.* **27**, 455–462 (1982)
46. Magde, D., Wong, R., Seybold, P.G.: Fluorescence quantum yields and their relation to lifetimes of rhodamine 6G and fluorescein in nine solvents: improved absolute standards for quantum yields. *Photochem. Photobiol.* **75**, 327–334 (2002)
47. Combariza, M.Y., Vachet, R.W.: The utility of ion-molecule reactions in a quadrupole ion trap mass spectrometer for analyzing metal complex coordination structure. *Anal. Chim. Acta.* **496**, 233–248 (2003)
48. Hashimoto, Y.: High sensitivity and broad dynamic range infrared multiphoton dissociation for a quadrupole ion trap. *Rapid. Commun. Mass. Spectrom.* **18**, 2255–2259 (2004)
49. Gudjons, T., Arbes, F., Benzing, M., Kurth, F., Werth, G.: Spatial fluorescence distribution and laser cooling of Ca^+ in a Paul trap. *Phys. Scr.* **T59**, 396–402 (1995)
50. Jensen, L., Schatz, G.C.: Resonance Raman scattering of rhodamine 6G as calculated using time-dependent density functional theory. *J. Phys. Chem. A.* **110**, 5973–5977 (2006)
51. Guthmuller, J., Champagne, B.: Resonance Raman scattering of rhodamine 6G as calculated by time-dependent density functional theory: vibronic and solvent effects. *J. Phys. Chem. A.* **112**, 3215–3223 (2008)
52. Kendrick, E.: A mass scale based on $\text{CH}_2=14.0000$ for high resolution mass spectrometry of organic compounds. *Anal. Chem.* **35**, 2146–2154 (1963)
53. Hughey, C.A., Hendrickson, C.L., Rodgers, R.P., Marshall, A.G., Qian, K.N.: Kendrick mass defect spectrum: a compact visual analysis for ultrahigh-resolution broadband mass spectra. *Anal. Chem.* **73**, 4676–4681 (2001)
54. Schmidt, J., Penzkofer, A.: Fluorescence spectroscopic investigations of rhodamine dye vapors. *Chem. Phys.* **133**, 297–301 (1989)
55. Dunbar, R.C.: Photodissociation in the ICR ion trap. In: Bowers, M.T. (ed.) Gas phase ion chemistry, vol. 3: ions and light. Academic, Orlando, FL (1984)
56. Kordel, M., Schooss, D., Neiss, C., Walter, L., Kappes, M.: Laser-induced fluorescence of rhodamine 6G cations in the gas phase: a lower bound to the lifetime of the first triplet state. *J. Phys. Chem. A.* **114**, 5509–5514 (2010)